Available online at www.sciencedirect.com

ScienceDirect

Procedia CIRP 94 (2020) 817–822

www.elsevier.com/locate/procedia

11th CIRP Conference on Photonic Technologies [LANE 2020] on September 7-10, 2020

Focus shift control of a novel 30 kW laser remote scanner for large-scale industrial sheet and plate metal applications

G. Cerwenka[a,*], J. Paternina[a], M. Elhefnawy[b], J. Wollnack[c], C. Emmelmann[a,b]

[a]*Fraunhofer Research Institution for Additive Manufacturing Technologies IAPT, Am Schleusengraben 14, 21029 Hamburg, Germany*
[b]*Institute of Laser and System Technologies (iLAS), Hamburg University of Technology (TUHH), Denickestraße 17, 21073 Hamburg, Germany*
[c]*Institute of Production Management and Technology (IPMT), Hamburg University of Technology (TUHH), Denickestraße 17, 21073 Hamburg, Germany*

* Corresponding author. Tel.: +49 40 484010 632; fax: +49 40 484010 999. *E-mail address:* georg.cerwenka@iapt.fraunhofer.de

Abstract

To overcome current limitations in laser remote processing of large-scale sheet and plate metal applications, an automated laser remote scanner (LRS) with a 30 kW laser power has been developed. Due to the high laser power, an unacceptable focus shift occurs at the processing location, mainly generated by the fused silica optics. A computationally efficient real-time focus shift compensation and control of the focus position have been investigated and are presented. In the first section, the 30 kW LRS concept is briefly introduced. Section two explains the focus shift effect and presents its impact on manufacturing scenarios in welding and cutting. The third section highlights significant effects accounted for: thermo-optical, stress-optical, geometric, and ambient. A set of simulated data of temperature, refractive index, and focus shift profiles have been generated in section four and model the performance of the 30 kW LRS. The results are discussed and a summary is given.

Keywords: 30 kW Laser Remote Scanner; Real-time; Focus Shift; Thermo-optical, Stress-optical, End Effect; Ambient Condition; Fused Silica, Welding, Cutting

1. Introduction

The laser remote scanner (LRS) technology is one of the most promising topics in industrial manufacturing [1]. There are an innumerable variety of applications [2-8]. The technology minimizes non-productive time and increases the production speed by up to 100 % [9, 10]. Besides that, it shows advantages for processing of structures that often have a high number of processing points widely distributed on the workpiece [11, 12]. LRS operate with large working distances of 300 mm to 1600 mm between the scanner head and the interaction zone [9, 11]. In combination with fiber-guided laser sources, the applicable plant engineering proves to be highly flexible [11, 13]. Particular engineering tasks in special purpose machinery, civil engineering, the rail vehicle industry, or in the maritime sector [2] can require laser powered LRS up to 30 kW or more. Nevertheless, no applications in large-scale industrial sheet and plate metal manufacturing are known, since LRS tools and their thermal control for variable power brilliant high-power laser beam sources are missing.

To overcome current limitations, a novel automated, single mirror-based, gimbal-mounted [14] LRS design for 30 kW laser power has been developed. The new approach eliminates size and weight constraints and reduces heat-induced focus shift effects in *f-Θ* lens implementations. The fused silica optics is designed for 1070 nm fiber laser sources, a fiber core diameter of 0.3 mm to 0.4 mm, and a magnification of 2:1. With a system focal length f_S of almost 1000 mm, the process area measures up to 900 · 900 mm² and the *z*-shift is 250 mm. This system includes a stereo camera-based 3D vision combined with a tailored image processing algorithm for part displacement detection as well as task estimation. The scanner controller manipulates a spot misalignment in real-time. The full 30 kW LRS concept description can be found in [15].

10.1016/j.procir.2020.09.118

However, brilliant high-power laser beam sources available today place high demands on the thermal stability of the optical elements in the 30 kW LRS and reveal the limits of conventional optical design. Time-dependent thermal effects lead to optical errors, such as focus shift Δz_F and aberrations, with its dependent process parameter changes, and have a significant influence on the processing result. [16-18] Considering the beam parameter product (BPP), a focus shift Δz_F of no more than 50 % of the measured optical system Rayleigh length $z_{R\,\sigma}$ is allowable to have empirically meaningful results [19, 20]. Thus, a focus shift control is developed and implemented for the 30 kW LRS.

2. Focus shift effect – impact on manufacturing scenarios

Based on high demands on the thermal load capacity of the optical elements in the 30 kW LRS, the bulk substrate must be optically pure, except for a small percentage of incorporated OH-ions, which are in the range from 800 ppm to 1200 ppm for fused silica standard grade [21-24]. Nevertheless, due to the absorption of a portion of the brilliant high-power laser radiation in the glass substrate, which is approx. 20 ppm · cm^{-1} for the applied fused silica Corning HPFS® 7980 standard grade [18, 25], and 95 ppm in the worst case of the applied AR coating /328 from Sill Optics, the optical elements heat up continuously. As a result, a radially- and time-dependent inhomogeneous temperature gradient $T(r,t)$ arises in the bulk substrate. $T(r,t)$ is dependent on the laser beam intensity distribution $I(r,t)$ on the irradiated surface, the absorbed part of the laser power $P_L(t)$ in the materials, and the duty cycle time t_{EM} of the laser beam emission. $T(r,t)$ is accompanied by refractive index and geometry changes of the optical elements, which lead to a focus shift Δz_F and beam aberrations. The higher the $P_L(t)$ and, thus, the laser beam-induced thermal behavior, the greater the effects on the focus properties. In summation, the focus geometry changes and beam brilliance and intensity losses occur.

As a result of the aforementioned negative influences process parameters get out of range, quality-based settings are lost, and finally, an unstable process occurs until the process stops. If an operator does not react promptly, in extreme cases, reject parts will result in an environment of frequently small batch sizes, whereby the sheet or plate material itself already represents a high cost factor. In a less extreme case, a high level of reworking and rectification work is time and cost intensive. At close inspection in high-power optics, the focus shift Δz_F reveals one of the main influences on the process result and the industrial process performance [26, 27]. [17] determine the focus shift Δz_F as the main factor for the observed change of the process result during the laser beam welding and [28] indicate for the cutting process that a focus position shortening of a lens of a few tenths of a millimeter can already show a negative influence. [18] describes comparable observations. If, in addition, highly reflective materials are processed, the thermally induced effect is increased by an increased thermal load due to a consequently lower absorption of the laser radiation with a simultaneously intensified back reflection [28].

3. Focus shift model theory and focus shift control

3.1. Background

An axially symmetrical optical elements arrangement is considered. The refractive index $n_{gl}(\lambda_0,T)$ of fused silica is temperature-dependent mainly corresponding to the "thermo-optical effect" with the thermo-optical coefficient $dn_{gl}/dT(r,t)$ or β and the "stress-optical effect" with the photo-elastic coefficients $dn_{gl\,\|/\perp}/d\sigma_T$ or $K_{\|/\perp}$ or the stress-optical coefficient $K = K_{\|} - K_{\perp}$, since $T(r,t)$ causes thermal stresses σ_T based on strain ε_T in the optical elements. An external mechanical force does not appear. The thermo-optical effect is mechanically strain- and stress-free [29]. Since heat-induced stresses σ_T reveal anisotropic glass properties even in isotropic bulk substrates, $n_{gl}(\lambda_0,T)$ depends on the plane of vibration of the laser beam parallel (||) and perpendicular (⊥) to σ_T [30, 31]. In the linear-elastic range, in addition to thermally induced mechanical strain effects, purely thermal strain effects occur in the axially symmetrical bulk substrate. They act during the fused silica-reversible heating and cooling process when interacting with the laser radiation. As a result, they lead to macroscopic geometric dimension changes, which actively support the focus shift Δz_F. Geometric changes are referred to as "end effect" and are changes in the thickness d of the optical elements and a deformation of the end face radii $R_{1/2}$. Hence, the optical path length (OPL) in the bulk substrate extends and, therefore, the absorption length as well. In addition, the surface refraction becomes lesser or stronger. All three effects together are termed as "thermal lens" and have the greatest impact on laser beam machining processes. Furthermore, the ambient conditions influence the free beam behavior of the laser beam as well as the transition between the propagation scenarios by the refractive index $n_{air}(\lambda_0)$ of air.

3.2. Refractive index

The thermal lens related radially- and time-dependent total refractive index $n_{abs\,gl\,\|/\perp}(r,t)$ is a linear combination of the reference refractive index $n_{abs\,0}(\lambda_0,T_0)$ and the refractive index change by β with $\Delta n_{abs\,T}$ and by $K_{\|/\perp}$ or K with $\Delta n_{abs\,\sigma T\,\|/\perp}$, all refractive indices with respect to vacuum, and is framed in the focus shift control model by the equation

$$n_{abs\,gl\,\|/\perp}(r,t) = n_{abs\,0}(\lambda_0,T_0) + \Delta n_{abs\,T} + \Delta n_{abs\,\sigma T\,\|/\perp}. \quad (1)$$

$n_{abs\,0}(\lambda_0,T_0)$ is given at the vacuum wavelength λ_0 for the isotropic bulk substrate and is computed from measurements performed by the glass manufactures [21, 23, 24] mostly at a reference temperature T_0 of 20 °C, a reference pressure p_0 of 101325 Pa, and a nitrogen (N_2) atmosphere with

$$n_{abs\,0}(\lambda_0,T_0) = n_{rel\,0}(N_2,\lambda_0,T_0)\cdot n_{N2}. \quad (2)$$

$\Delta n_{abs\,T}$ is extracted by the Sellmeier dispersion equation-based extended formula

$$\Delta n_{abs\,T} = \frac{n_{abs\,0}^2-1}{2n_{abs\,0}}\cdot\left(D_0 + D_1\Delta T + D_2\Delta T^2 + \frac{E_0+E_1\Delta T}{\lambda_0^2-\lambda_{TK}^2}\right)\Delta T \quad (3)$$

[30, 32-34] as fitted values in the expected temperature range with $\Delta T = T(r,t) - T_0$, where $T(r,t)$ has to be closed integrable. D_0, D_1, D_2, E_0, E_1, and λ_{TK} are the six fit constants taken from the datasheets of the glass manufacturers. The determination of $\Delta n_{\mathrm{abs}\,\sigma T\,\parallel/\perp}$ is performed by the formula set

$$\begin{bmatrix}\Delta n_{\mathrm{abs}\,\sigma T\,\parallel}\\ \Delta n_{\mathrm{abs}\,\sigma T\,\perp}\end{bmatrix} = K_{\parallel}\cdot\begin{bmatrix}\sigma_{T\,rr}(r)\\ \sigma_{T\,\varphi\varphi}(r)\end{bmatrix} + K_{\perp}\cdot\begin{bmatrix}\sigma_{T\,\varphi\varphi}(r)\\ \sigma_{T\,rr}(r)\end{bmatrix}, \tag{4}$$

where $\sigma_{T\,rr}(r)$ and $\sigma_{T\,\varphi\varphi}(r)$ are the heat-induced radial and tangential principal stresses, respectively depending on the radial position r in the optical element explained by [30-32, 34]. Row one describes the arising $\Delta n_{\mathrm{abs}\,\sigma T}$ $\parallel$ to $\sigma_{T\,rr}(r)$ and $\perp$ to $\sigma_{T\,\varphi\varphi}(r)$ and row two depicts $\Delta n_{\mathrm{abs}\,\sigma T}$ $\perp$ to $\sigma_{T\,rr}(r)$ and $\parallel$ to $\sigma_{T\,\varphi\varphi}(r)$. $K_{\parallel}$ and $K_{\perp}$ are estimated on existing values of the piezo-optical coefficients q_{11} and q_{12} [30, 35] or stress-optical coefficient K [31], given in the glass datasheets, by

$$\begin{bmatrix}K_{\parallel}\\ K_{\perp}\end{bmatrix} = -\frac{n_{\mathrm{abs}\,0}^3}{2}\cdot\begin{bmatrix}q_{11}\\ q_{12}\end{bmatrix} = \frac{n_{\mathrm{abs}\,0}^2-1}{2n_{\mathrm{abs}\,0}}\cdot\frac{1-2\nu}{\mathrm{E}} - \frac{1}{1+\nu}\cdot\begin{bmatrix}-K\\ \nu\cdot K\end{bmatrix} \tag{5}$$

with the material-specific elasticity modulus E as well as the transverse contraction coefficient ν. Considering a parabolic approximation of $T(r,t)$ the principal stresses $\sigma_{T\,rr}(r)$ and $\sigma_{T\,\varphi\varphi}(r)$ are expressed by

$$\sigma_{T\,rr}(r) = \frac{X}{4}\cdot\begin{cases}\left[4\ln\left(\frac{r_B}{r_L}\right) - \left(\frac{r_B}{r_L}\right)^2 + \left(\frac{r}{r_B}\right)^2\right], & r \le r_B\\ \left[4\ln\left(\frac{r}{r_L}\right) - \left(\frac{r_B}{r_L}\right)^2 + \left(\frac{r_B}{r}\right)^2\right], & r > r_B\end{cases}$$

$$\sigma_{T\,\varphi\varphi}(r) = \frac{X}{4}\cdot\begin{cases}\left[4\ln\left(\frac{r_B}{r_L}\right) - \left(\frac{r_B}{r_L}\right)^2 + 3\left(\frac{r}{r_B}\right)^2\right], & r \le r_B\\ \left[4\ln\left(\frac{r}{r_L}\right) - \left(\frac{r_B}{r_L}\right)^2 - \left(\frac{r_B}{r}\right)^2 + 4\right], & r > r_B\end{cases} \tag{6}$$

[36], where $X = \mathrm{E}\cdot\overline{\alpha_L}\cdot\Delta T$ and $\overline{\alpha_L}$ terms the average linear coefficient of thermal expansion (CTE) of the quantity $0.57\cdot10^{-6}\,\mathrm{K}^{-1}$ for a temperature range of 0 °C to 200 °C of Corning HPFS® 7980. Furthermore, r_L is the lens radius and r_B is the radius of the impinging laser beam. For deeper insights on the general focus shift control model consult [15].

3.3. Geometry

The revealed volume aggregation is considered in the focus shift control model by a simplified scalable volume equation in respect to the optical element shape explained in [15] and the applied laser beam intensity distribution $I(r,t)$ with an extension of this equation by two adaption factors a and b. The integrated equation of the demanded new thickness $d(r,T)$ with respect to the element radius r_L by a and b has the form

$$d(r,T) = \left[\frac{3}{2}\cdot\frac{e^{(3\,\overline{\alpha_L}\cdot\Delta T)}-1}{(a+b)^2-a\cdot b} + 1\right]\cdot d(T_0), \tag{7}$$

where a and b are the proportions between the surface radii $r_{t/b}$ of the additional scalable volume shape tops (t) and bottoms (b). The calculation of the new end face radii $R_{1/2}$ is described in reference [15].

3.4. Ambient Condition

The transition between glass and ambient is always dependent on the refractive index of the ambient, which is mainly air and the ambient medium of the 30 kW LRS optics. Due to this fact it is essential to know their condition very well. $n_{air}(\lambda_0)$ is significantly influenced by three main ambient quantities: 1) temperature T_U; 2) pressure p_{abs}; 3) water vapor (wv) partial pressure e in dependency of relative humidity rH. Moreover, the pollution of air has to be taken into account, mostly the 4) CO_2 content x_{CO2}. Another demanding quantity is the 5) vacuum wavelength λ_0 of the relevant radiation. References presenting more insights on the topic are [32, 37-44]. The relation between e and rH is documented in [44, 45]. T_U exerts the greatest influence. The dependencies for $n_{air}(\lambda_0)$ are noted in the focus shift control model by the relationship of [39-41], termed

$$n_{\mathrm{air}} = 1 + (n_{\mathrm{air\,xCO2\,s}} - 1)\frac{\rho_{\mathrm{air}}}{\rho_{\mathrm{air\,xCO2\,s}}} + (n_{\mathrm{wv\,s}} - 1)\frac{\rho_{\mathrm{wv}}}{\rho_{\mathrm{wv\,s}}}. \tag{8}$$

Eq. (8) is based on information of different refractive indices n and densities ρ at two main air conditions. The air states are essentially divided into what is by definition a so-called "standard condition" (s) of the ambient air [37, 38, 46] and into a current ambient air condition. At the end, a transformation between $n_{\mathrm{abs\,gl}\,\parallel/\perp}(r,t)$ (cf. Eq. (1)) and $n_{\mathrm{rel\,gl}\,\parallel/\perp}(r,t)$ with respect to air with $n_{air}(\lambda_0)$ by Eq. (8) is performed similar to Eq. (2).

3.5. Focus shift control

A constant focus position relative to the workpiece surface and accompanying important laser beam parameters, such as intensity and focus geometry, contribute to a requirement-related processing quality. This task is performed by the designed focus shift control method. Based on the pose set point of the preset focus position z_F, the knowledge of the optics design, and its internal behavior (cf. Sect. 4.2) the integrated algorithms react to time-dependent changes of the laser-beam-loaded 30 kW LRS optical system and its recorded ambient conditions. Fig. 1 shows the schematic of the correction principle.

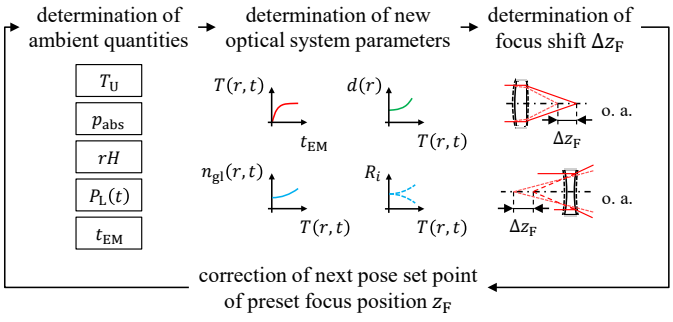

Fig. 1. Schematic of the correction principle of the focus shift Δz_F. The quantities T_U, p_{abs}, rH, $P_L(t)$, and t_{EM} indicate the ambient temperature, pressure, and relative humidity as well as the optical power and the duty cycle time of the laser beam emission; o. a. describes the optical axis.

An underlying temperature model forms the starting point for the determination of the temperature-dependent change of the refractive index $n_{gl}(\lambda_0,T)$ and the optical element geometry. In order to map the heat transfer processes over the entire lens radius as a function of the impinging laser radiation, the temperature model is framed on the finite element method (FEM). Any intensity profiles, the superimposition of the energy input, and the energy dissipation for arbitrary lens sections as well as time intervals can be calculated. An adopted ABCD matrix formalism models the optical system and allows a fast, computer-aided calculation for the complex optics design of the 30 kW LRS. Further information on the theoretical and mathematical design plus the assumed boundary conditions of the model is given in [15]. Moreover, the focus shift control model is directly connected to the captured ambient condition with its quantities pictured in Fig. 1. The equation

$$\Delta z_F = -\frac{B_{OS\,th}}{D_{OS\,th}} + \frac{B_{OS}}{D_{OS}} \tag{9}$$

expresses the focus shift Δz_F along the optical axis by the matrix elements B_{OS} and D_{OS} of the system optics matrix (OS), which is described in [15]. The first term represents the system focus position $z_{F\,th}$ under thermal load (th) and the second term is the original preset system focus position z_F. If $\Delta z_F < 0$ the system focal length f_S gets shorter. If $\Delta z_F > 0$ the system focal length f_S extends. Based on the strength of Δz_F, the correction of the next pose set point of the preset focus position z_F will be estimated. In addition, out of that the shift s_z of the sliding lens is determined. All in all that allows a computer-aided real-time correction of the focus position z_F in one deterministic cycle time step.

4. Selected aspects of the focus shift control model

4.1. Boundary conditions

For the three simulation scenarios: 1) temperature behavior, 2) refractive index behavior, 3) focus shift behavior, all lenses in the 30 kW LRS optics setup consist of fused silica Corning HPFS® 7980 standard grade, are firmly clamped in separate holders over the entire lateral surface, and have the reference ambient temperature T_U at the interface with the mounts. Mirrors are neglected. $n_{abs\,0}(\lambda_0,T_0)$ is calculated as explained in Sec. 3.2 and is rounded off to 1.449995. Axial forces and stresses are not considered, since a top-hat laser beam with homogeneous intensity is assumed along the optical axis. An axial temperature gradient does not occur. The applied laser source is an IPG Ytterbium fiber laser with $P_L(t) \leq 30$ kW and $\lambda_0 = 1070$ nm ± 10 nm as well as a BPP ≤ 18 mm · mrad. All estimates are conducted at different laser powers $P_L(t)$: 2 kW, 10 kW, 20 kW, and 30 kW. The temperature behavior is extracted over a realistic lasing process time t_{EM} of 10 s. Both refractive index and focus shift behaviors are calculated over a lasing time t_{EM} of 600 s. This period is chosen in the interest of greater clarity of the results. Processes with a corresponding processing time with a continuous wave of 30 kW laser power are unrealistic for LRS systems.

4.2. Temperature, refractive index, and focus shift behaviors

The presented aspects of the focus shift control model have been carried out by a study of simulated temperature and refractive index profiles for the first single collimation lens in an exemplary fashion, considering Sec. 4.1. The lens radius r_L is 26 mm, and the radius r_B of the impinging laser beam measures 17.6 mm in the plane of the half lens thickness d. Fig. 2 frames the results of four temperature change profiles ΔT against the radius r at different laser powers up to $P_L(t) = 30$ kW.

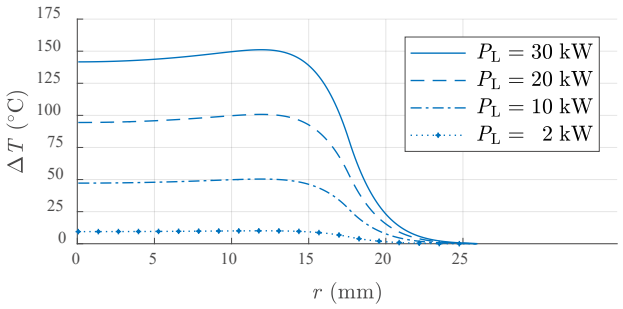

Fig. 2. Different temperature change profiles ΔT after $t_{EM} = 10$ s at different laser powers $P_L(t)$ for the first single collimation lens in the 30 kW LRS optics setup starting from an ambient temperature $T_U = 20$ °C.

The plotted curves are calculated by the implemented FEM-based temperature model, and they are the result of all three heat transfer aspects: 1) heat conduction; 2) heat convection; 3) heat radiation, where heat conduction represents the highest heat transfer through the lens to the mount. It can be shown, that for $P_L(t) = 30$ kW a temperature difference ΔT of approx. 151 °C prevails inside the lens at around 46 % of r_L and at around 68 % of r_B after $t_{EM} = 10$ s. The temperature difference ΔT in the center of the lens is 9.5 °C less. Furthermore, Fig. 2 represents the intensity distribution of the top-hat laser radiation and additionally shows the heat build-up towards the lens edge before sufficient heat dissipation via the mount at $r = 26$ mm takes place. As a result, the laser beam is refracted more strongly in this lens area than near the center, and focus aberrations occur.

Fig. 3 gives an impression on the change of $\overline{n_{rel\,gl}}(\lambda_0,T)$ – as mean value of $n_{rel\,gl\,\parallel}(\lambda_0,T)$ and $n_{rel\,gl\,\perp}(\lambda_0,T)$ (difference ≤ 10^{-9}) – with respect to $n_{air}(\lambda_0)$ by Eq. (8) over a lasing time t_{EM} of 600 s at different laser powers $P_L(t)$ with reference to Sec. 4.1.

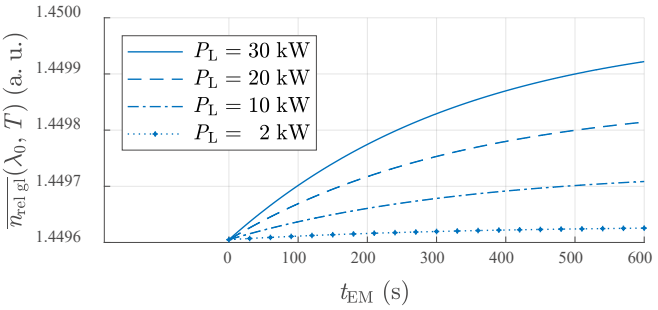

Fig. 3. Mean refractive index curves $\overline{n_{rel\,gl}}(\lambda_0,T)$ after $t_{EM} = 600$ s at different laser powers $P_L(t)$ for the first single collimation lens in the 30 kW LRS optics setup starting from an ambient temperature $T_U = 20$ °C.

It can be stated, that $n_{\text{rel gl}}(\lambda_0,T)$ changes by approx. $32 \cdot 10^{-5}$ at $P_L(t) = 30$ kW and after $t_{EM} = 600$ s. Together with geometrical changes, a $\overline{\Delta z_F}$ – as mean value of ∥ and ⊥ focus shift by $n_{\text{rel gl}\,\parallel/\perp}(\lambda_0,T)$ – of around $-136.2 \cdot 10^{-3}$ mm results for the first collimation lens based on Eq. (9), in which $\overline{\Delta z_F}$ shows a linear dependence on $\overline{n_{\text{rel gl}}}(\lambda_0,T)$ over the entire $P_L(t)$ range. The thermo-optical effect (cf. Eq. (3)) contributes 98.96 % of the refractive index change, whereas the stress-optical effect (cf. Eq. (4)) only provides 1.04 %. Furthermore, already a realistic exposure time t_{EM} of 10 s of a laser radiation $P_L(t)$ of 30 kW leads to a $\overline{\Delta z_F}$ of approx. $-4.7 \cdot 10^{-3}$ mm, which results in a shorter focal length f_{L1} of the first lens.

In addition, the mean focus shift behavior is documented for the entire 30 kW LRS optics setup in Fig. 4.

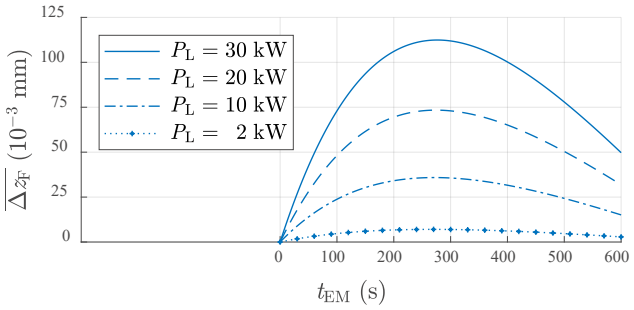

Fig. 4. Mean focus shift $\overline{\Delta z_F}$ against time t_{EM} over a lasing period of 600 s at different laser powers $P_L(t)$ for the 30 kW LRS optics setup starting from an ambient temperature $T_U = 20$ °C.

It provides an impression of the change of the focus position z_F against $P_L(t)$ and after $t_{EM} = 600$ s, expressed by a predicted mean focus shift $\overline{\Delta z_F}$ of only approx. $49.7 \cdot 10^{-3}$ mm at $P_L(t) = 30$ kW. Nevertheless, the $\overline{\Delta z_F}$ according to the curves between 200 s and 400 s is quite large compared to the other extracted values and is rounded off to $112.4 \cdot 10^{-3}$ mm. In a reasonable process time t_{EM} of a few seconds up to 30 s the $\overline{\Delta z_F}$ is no more than $26.9 \cdot 10^{-3}$ mm. That small $\overline{\Delta z_F}$ occurs solely because the 30 kW LRS optical system is very well balanced in its design. Care has been taken to ensure that the optical lens properties compensate each other in the best possible way. All $\overline{\Delta z_F}$ values are positive within $t_{EM} = 600$ s and thus, the focal length f_S increases. The reason for that is a different time constant for the heating process of the different lenses in the 30 kW LRS optics setup. The sliding lens, which is a concave lens, is thinner than all other lenses and heats up faster. About 759 s after the start of the laser radiation, the different lenses have almost compensated the mean focus shift $\overline{\Delta z_F}$. As a result of the focus shift Δz_F, the correction of the next pose set point of the preset focus position z_F is estimated by the focus shift control method and an updated sliding lens position is given.

The presented results give the assumption that a focus position correction is a fine adjustment of the focus position z_F. Ideally, the change of z_F shows only a slight change of the laser beam and process parameters. However, it must be noted, that no degree of contamination of the lens surfaces has yet been considered, as may well be the case with the protective glass. In the case of contamination, z_F can change more and more, since an increasingly higher absorption occurs.

5. Conclusion

This paper briefly has introduced a novel 30 kW laser remote scanner design approach for large-scale applications. It combines an optics solution with intermediate foci and a gimbal-mounted single scanning mirror for up to 30 kW laser power. The integrated stereo camera system leads to a self-teaching automated LRS system. Furthermore, to compensate the effect of focus shift Δz_F and to control the focus position z_F for variable power brilliant high-power laser beam LRS systems a computational solution has been presented. Hence, the main physical effects on the focus shift Δz_F for optical lenses and their implementation in the focus shift control model have been explained. In addition, selected aspects of the focus shift control model at different laser powers $P_L(t)$ for the 30 kW LRS optical system have been studied, which are a set of simulated data of temperature and mean refractive index profiles for the first single collimation lens in an exemplary fashion as well as mean focus shift profiles of the entire optical system. It can be stated, that the FEM-based thermal model provides a good estimation of the temperature profiles over the entire lens diameter. It is shown, that already a realistic exposure time t_{EM} of 10 s of a laser radiation of 30 kW leads to a ΔT of approx. 151 °C at around 46 % of the lens radius r_L and thus, a $\overline{\Delta z_F}$ of around $-4.7 \cdot 10^{-3}$ mm, which results in a shorter focal length f_{L1} of the first lens. The laser beam is more strongly refracted in the area with the highest ΔT than near the lens center and focus aberrations will appear. Moreover, the mean focus shift $\overline{\Delta z_F}$ shows a linear dependence of $\overline{n_{\text{rel gl}}}(\lambda_0,T)$ over the entire $P_L(t)$ range. The contribution to the change of the refractive index by the thermo-optical and the stress-optical effect is 98.96 % and 1.04 %, respectively. In addition, a mean focus shift quantity of the entire 30 kW LRS optical system has been predicted. In a reasonable process time t_{EM} of a few seconds up to 30 s the mean focus shift $\overline{\Delta z_F}$ is no more than $26.9 \cdot 10^{-3}$ mm. However, it must be noted, that no degree of contamination of the protective glass has yet been considered. z_F can change more and more, since an increasingly higher absorption occurs. In summation, the presented computer-based solution provides an appropriate overview of the heat-induced temperature-dependent optical and mechanical effects in the novel high-power 30 kW laser remote scanner and gives an estimation about the expected essential quantities. The focus position control method in the 30 kW LRS is suitable for predicting the focus behavior and is a method that allows fine adjustment of the focus position z_F in accordance with the sliding lens of the mechanical scanner setup.

Acknowledgements

This research was kindly funded by the German Federal Ministry for Economic Affairs and Energy (BMWi) after a decision of the Deutsche Bundestag within the framework of the research project “QuInLas” and “ShipLight”. We acknowledge the support of our colleagues and project partners who provided insight and expertise that greatly assisted the research. We thank our scientific assistants.

References

[1] Katayama S. Introduction: fundamentals of laser welding. In: Katayama S, editor. Handbook of laser welding technologies. 1st ed. Oxford Cambridge Philadelphia New Delhi: Woodhead Publishing Ltd; 2013. pp. 3-16.

[2] Emmelmann C, Wollnack J, Kirchhoff M, Beckmann F, Cerwenka G. Application of the laser remote welding technology with 3D sensors in ship and civil engineering. In: Proceedings of the 66th IIW International Conference on "Automation in Welding". Essen; 2013.

[3] Wetzig A, Baumann R, Herwig P, Siebert R, Beyer E. Laser remote cutting of metallic materials: opportunities and limitations. In: SPIE Proceedings 9657. Kenilworth; 2015. pp. 965708-1-965708-5.

[4] Herzog D, Schmidt-Lehr M, Oberlander M, Canisius M, Radek M, Emmelmann C. Laser cutting of carbon fiber reinforced plastics of high thickness. Materials & Design 2016; 92: pp. 742-749.

[5] Gebhardt A. Additive Fertigungsverfahren. Additive Manufacturing und 3D-Drucken für Prototyping – Tooling – Produktion. 5th ed. Munich: Carl Hanser Verlag; 2016.

[6] Cerwenka G, Surrey P, Möller M, Conrad C, Prakash V, Heilemann M, Emmelmann C. In-depth characterization of the scanner-based selective laser deburring process. JLA 2018; 30(3): pp. 032510-1-032510-9.

[7] Hans B. The Audi e-tron. In: Proceedings of the Joining in car body engineering. Detroit; 2020.

[8] Zhang W. Remote laser welding of closure and battery tray in Gestamp. In: Proceedings of the Joining in car body engineering. Detroit; 2020.

[9] Zäh MF, Moesl J, Musiol J, Oefele, F. Material processing with remote technology revolution or evolution? Physics Procedia 2010; 5(A): pp. 19-33. Doi: 10.1016/j.phpro.2010.08.119.

[10] Wetzig A. Developments in beam scanning (remote) technologies and smart beam processing. In: Katayama S, editor. Handbook of laser welding technologies. 1st ed. Oxford Cambridge Philadelphia New Delhi: Woodhead Publishing Ltd; 2013. pp. 422-433.

[11] Thomy C, Grupp M, Seefeld T, Sepold G, Vollertsen F. CO_2-Laser-Remoteschweißen. Grundlagen, Prozessuntersuchungen und Anwendungen. wt Werkstattstechnik online 2004; 94(7/8): pp. 373-378.

[12] Tsoukantas G, Chryssolouris G. Theoretical and experimental analysis of the remote welding process on thin, lap-joined AISI 304 sheets. Int J Adv Manuf Technol 2008; 35(9-10): pp. 880-894. Doi: 10.1007/s00170-006-0767-0.

[13] Kah P, Lu J, Martikainen J, Suoranta R. Remote Laser Welding with High Power Fiber Lasers. Engineering 2013; 05(09): pp. 700-706. Doi: 10.4236/eng.2013.59083.

[14] Munsch M, Wollnack J, Kirchhoff M, Emmelmann C. Parallelkinematisches Spiegel-Ablenksystem mit doppelkardanischer Aufhängung, DE102012012780 A1, WO2014000883 A1. 26.06.2012.

[15] Cerwenka G, Wollnack J, Krähling T, Jayaprakash R, Emmelmann C. 3D/6D calibration and real-time focus shift compensation for automated 30 kW laser remote scanner. JLA 2019; 31(2): pp. 022607-1-022607-9. Doi: 10.2351/1.5096135.

[16] Märten O, Kramer R, Schwede H, Wolf S, Brandl V. Fokusanalyse. Charakterisierung von Fokussierungssystemen für Hochleistungslaser mit hoher Strahlqualität (Teil 1). Laser + Photonics 2008; 2: pp. 48-51.

[17] Reitemeyer D, Seefeld T, Vollertsen F, Bergmann JP. Influences on the laser induced focus shift in high power fiber laser welding. In: Proceedings of the 5th LiM Laser in Manufacturing. München; 2009. pp. 293-298.

[18] Kugler T. Maximum uptime and minimum focus shift in high-power 1µm laser beam delivery. In: SPIE Proceedings 8239. San Francisco; 2012. pp. 82390X-1-82390X-9. Doi: 10.1117/12.908830.

[19] Bisson JF, Sako H. Suppression of the Focal Shift of Single-Mode Laser with a Miniature Laser Processing Head. JLMN 2009; 4(3): pp. 170-176. Doi: 10.2961/jlmn.2009.03.0005.

[20] Kögel G. High-Power-Scanning. Scanner erobern immer weitere Anwendungen und beherrschen größte Leistungen und höchste Präzision. EuroLaser 2011; 4: pp. 28-31.

[21] SCHOTT Lithotec AG. Synthetic Fused Silica. DUV/UV, VIS and IR applications. Jena; 2006.

[22] De Jong BHWS, Beerkens RGC, van Nijnatten PA, Le Bourhis E. Glass, 1. Fundamentals. In: Elvers B editor. ULLMANN'S Encyclopedia of Industrial Chemistry. 7th ed. Weinheim: WILEY-VCH Verlag GmbH & Co. KGaA; 2011. p. 11.

[23] Corning Incorporated. Corning HPFS® 7979, 7980, 8655 Fused Silica. Optical Materials Product Information, Specialty Materials Division. New York; 2014.

[24] Heraeus Quarzglas GmbH & Co. KG. Quartz Glass for Optics. Data and Properties. Hanau; 2018.

[25] Carpenter DT, Wood CS, Lyngnes O, Traggis NG. Ultra low absorption glasses and optical coatings for reduced thermal focus shift in high power optics. In: SPIE Proceedings 8239. San Francisco; 2012. pp. 82390Y-1-82390Y-9. Doi: 10.1117/12.905462.

[26] Blomster O, Pålsson M, Roos SO, Blomqvist M, Abt F, Dausinger F, Deininger C, Huonker M. Optics performance at high-power levels. In: SPIE Proceedings 6871. San Jose; 2008. pp. 68712B-1- 68712B-10. Doi: 10.1117/12.762954.

[27] Scaggs M, Haas G. Thermal lensing compensation optics for high power lasers. In: SPIE Proceedings 7913. San Francisco; 2011. pp. 79130C-1-79130C-9. Doi: 10.1117/12.871370.

[28] Hügel H, Graf T. Laser in der Fertigung. Grundlagen der Strahlquellen, Systeme, Fertigungsverfahren. 3rd ed. Wiesbaden: Springer Vieweg; 2014. p. 85.

[29] Davis MJ, Hayden JS.: Thermal Lensing of Laser Materials. In: SPIE Proceedings 9237. Boulder; 2014. pp. 923710-1-923710-13.

[30] Hoffmann HJ. 2.4 Differential Changes of the Refractive Index. In: Bach H, Neuroth N, editors. The Properties of Optical Glass, Schott Series on Glass and Glass Ceramics. Berlin Heidelberg: Springer-Verlag; 1998. pp. 104-114.

[31] SCHOTT AG. TIE-27: Stress in optical glass. Mainz; 2019. pp. 4-5.

[32] Hoffmann HJ. 5. Optische Werkstoffe. In: Litfin G, editor. Technische Optik in der Praxis, 3rd ed. Berlin Heidelberg New York: Springer-Verlag; 2005. pp. 128-133, 144-149.

[33] SCHOTT AG. TIE-19: Temperature Coefficient of the Refractive Index. Mainz; 2016. pp. 1-3.

[34] Gatej A. Modeling and Compensation of Thermally Induced Optical Effects in Highly Loaded Optical Systems. Dissertation. RWTH Aachen. Aachen; 2014. pp. 15-16.

[35] Klein CA. Optical distortion coefficients of high-power laser windows. Optical Engineering 1990; 29(4): pp. 343-350.

[36] Cousins, AK. Temperature and thermal stress scaling in finite-length end-pumped laser rods. IEEE J Quantum Electronics 1992; 28(4): pp. 1057-1069. Doi: 10.1109/3.135228.

[37] Birch KP, Downs MJ. An Updated Edlén Equation for the Refractive Index of Air. Metrologia 1993; 30(3): pp. 155-162. Doi: 10.1088/0026-1394/30/3/004.

[38] Rosenbruch KJ. 6.1.1.2 Brechungs- und Reflexionsgesetz. In: Kohlrausch F, Kose V, Wagner S, editors. Praktische Physik. Zum Gebrauch für Unterricht, Forschung und Technik (Band 2). 24th ed. Stuttgart: B. G. Teubner Stuttgart; 1996. p. 95.

[39] Ciddor PE. Refractive index of air: new equations for the visible and near infrared. Applied Optics 1996; 35(9): pp. 1566-1573.

[40] Ciddor PE. Refractive index of air: 3. The roles of CO_2, H_2O, and refractivity virials. Applied Optics 2002; 41(12): pp. 2292-2298.

[41] Ciddor PE. Refractive index of air: 3. The roles of CO_2, H_2O, and refractivity virials: erratum. Applied Optics 2002; 41(33): p. 7036.

[42] Meiners-Hagen K, Pollinger F, Abou-Zeid A. Brechzahlkompensation mittels Mehrwellenlängen-Interferometrie. PTB-Mitteilungen 2010; 120(2): pp. 110-114.

[43] Rahneberg I. Untersuchungen zu optischen Mehrkomponentenmesssystemen. Dissertation. TU Ilmenau. Ilmenau; 2013. pp. 49-50.

[44] Dvořáček F. Survey of Selected Procedures for the Indirect Determination of the Group Refractive Index of Air. J Adv Eng 2018; 58: pp. 9-16.

[45] Manfred Zeller M, Busweiler U. M8 Be- und Entfeuchten von Luft. In: VDI-Gesellschaft Verfahrenstechnik und Chemieingenieurwesen (VDI-GVC) editor. VDI-Wärmeatlas. 11th ed. Berlin Heidelberg: Springer-Verlag; 2013. p. 1535.

[46] DIN Deutsches Institut für Normung e. V. Referenzzustand, Normzustand, Normvolumen - Begriffe und Werte (DIN 1343:1990-01). Berlin Wien Zürich: Beuth Verlag GmbH; 1990.